Nanoalloy Printed and Pulse-Laser Sintered Flexible Sensor Devices with Enhanced Stability and Materials Compatibility

Wei Zhao,[†] Thomas Rovere,[†] Darshana Weerawarne,[‡] Gavin Osterhoudt,[‡] Ning Kang,[†] Pharrah Joseph,[†] Jin Luo,[†] Bonggu Shim,[‡] Mark Poliks,[§] and Chuan-Jian Zhong*[,†]

[†]Department of Chemistry, [‡]Department of Physics, and [§]Department of System Science and Industrial Engineering, State University of New York at Binghamton, Binghamton, New York 13902, United States

ABSTRACT While conformal and wearable devices have become one of the most desired formats for printable electronics, it is challenging to establish a scalable process that produces stable conductive patterns but also uses substrates compatible with widely available wearable materials. Here, we describe findings of an investigation of a nanoalloy ink printed and pulsed-laser sintered conductive patterns as flexible functional devices with enhanced stability and materials compatibility. While nanoparticle inks are desired for printable electronics, almost all existing nanoparticle inks are based on single-metal component, which, as an electronic element, is limited by its inherent stabilities of the metal such as propensity of metal oxidation and mobility of metal ions, especially in sintering processes. The work here has demonstrated the first example in exploiting plasmonic coupling of nanoalloys and pulsed-laser energy with controllable thermal penetration. The experimental and theoretical results have revealed clear correlation between the pulsed laser parameters and the nanoalloy structural characteristics. The superior performance of the resulting flexible sensor device, upon imparting nanostructured sensing materials, for detecting volatile organic compounds has significant implications to developing stable and wearable sensors for monitoring environmental pollutants and breath biomarkers. This simple "nanoalloy printing—laser sintering—nanostructure printing" process is entirely general to many different sensor devices and nanostructured sensing materials, enabling the ability to easily construct sophisticated sensor array.

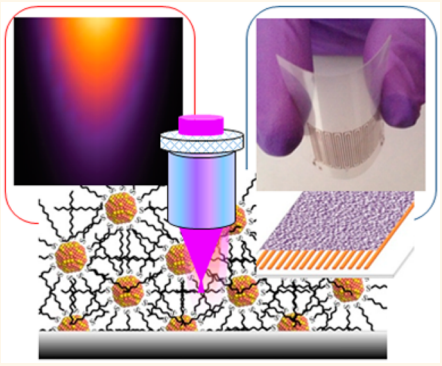

KEYWORDS: nanoalloy · nanoink · pulsed -laser sintering · printed flexible device · nanostructured sensing thin films · wearable sensor · printed electronics

Conformal and flexible devices have become an increasingly popular format for portable electronics such as sensors, smart phones, waist monitors, and wearable medical patches.[1−8] A fully digital, maskless, low-temperature, and fast-printing method represents a desired approach to manufacturing such portable electronics.[2−4] One of the rapidly emerging approaches is printing metal nanoparticle inks on polymeric materials,[9−11] followed by an effective sintering process. While nanoparticle inks are desired for printable electronics, all existing nanoparticles inks are based on single-metal component. As an electronic element, the stability of single-metal based nanoparticle inks is limited by its inherent stabilities of the metal such as propensity of metal oxidation and mobility of metal ions, especially in thermal or laser sintering processes. In comparison with conventional thermal sintering,[12] laser sintering has received increasing interests largely because of its controllable thermal penetration and low-temperature processing attributes.[3,10,13,14] Laser sintering of certain metal nanoparticles is very efficient due to surface plasmon resonance,[15,16] as documented by studies of visible radiation of gold nanoparticles at surface plasmon resonant frequencies leading to thermal energy in proportion to incident laser power,[15] and temperature rise of metal nanoparticles scaling with the particle size ($\Delta T_{max} \propto R^2_{NP}$).[16] For copper- or silver-based nanoparticle printed substrate,[10] obtaining

* Address correspondence to cjzhong@binghamton.edu.

Received for review March 8, 2015 and accepted May 28, 2015.

Published online June 02, 2015
10.1021/acsnano.5b02704

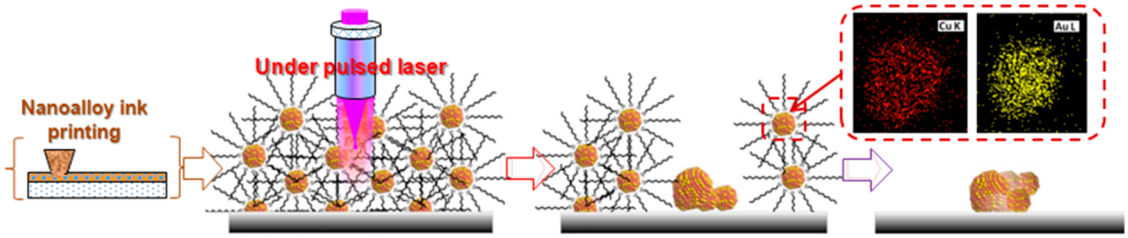

Figure 1. Nanoink printing and pulsed-laser sintering lead to the formation of conductive pattern on a substrate (Inset image: composition mapping of a single $Cu_{53}Au_{47}$ NP showing a uniform distribution of the two metal components across the alloy NP).

highly conductive patterns by thermal or laser sintering requires nitrogen or hydrogen atmosphere to decrease their oxidation,[17] or minimizing the mobility of silver ions.[18] In comparison with traditional thermal sintering, continuous wave and pulsed-laser sintering of silver or copper nanoparticle (NP) inks[19−21] have demonstrated increasing promises for manufacturing flexible electronics,[2,3] where the laser-induced heating is highly localized and the "digital" nature of the pulsed laser removes the need for expensive photomasks and allows easy design modification and fast 2D/3D fabrication on large-area polymeric materials. However, none of the existing approaches effectively address the propensity of metal oxidation or the mobility of metal ions during the sintering processes, which leads to the ultimate degradation in the printed electronics.[11] Data for most studies of laser sintering or thermal sintering were obtained under inert or reductive atmosphere or with certain reactive additives in the nanoinks for subsequent reduction of the oxidized metals after sinteting.[22−24] This problem is partly reflected by the fact that few studies of the laser-sintered inks have demonstrated the viability as functional flexible devices with sufficient stability on conventional materials.

Here, we describe a new combination of nanoalloy inks with pulsed-laser sintering for the fabrication of electrode patterns embedded in a flexible chemical sensor with enhanced stability and materials compatibility for the detection of environmental pollutants and breath biomarkers. In contrast to laser sintering of pure metal nanomaterials, laser sintering of nanoalloy inks is, to our knowledge, demonstrated for the first time. This combination offers entirely new attributes that the existing laser sintering of pure metal nanoparticles cannot achieve. In comparison with existing laser sintering of pure metal nanoparticles, laser sintering of nanoalloys enables enhanced stability against the propensity of oxidation metal components and sintering at lower melting point, which are two of the most important parameters in expanding the laser sintering technology to practical application to a variety of different flexible or wearable substrates. This new strategy allows nanoink-printed and laser-sintered flexible sensor devices with stable conductive electrodes and conventional materials compatible substrates (*e.g.*, regular plastic or glass materials). While this strategy is entirely general, it is demonstrated here by alloying copper with gold in different percentages. It is known that alloying copper with a certain percentage of oxidation-resistant or structure-stabilizing metal components (*e.g.*, Al, Ni) features the capability preventing copper from oxidation which is essential in device functional applications.[25] CuAu nanoalloy is exploited as a model system of nanoalloy inks mainly because of its increased stability as demonstrated for thermal sintering.[26] The coupling of the nanoalloy inks with pulsed-laser sintering is demonstrated for the fabrication of flexible chemical sensors,[27,28] which represents an intriguing pathway toward manufacturing wearable electronic devices.[29]

RESULTS AND DISCUSSION

As illustrated in Figure 1, the pulsed-laser sintering of the printed nanoalloy inks enables the ability to create a conductive pattern or footprint on a substrate with a controllable thermal penetration. In contrast to single-component copper and silver based nanoparticles as inks, alloys with a small fraction of gold offer an enhanced stability. Nanoalloys (Cu_nAu_{100-n}) with controllable size and composition[20,21] serve as ideal printable nanoinks since air-stable and larger-sized alloy nanoparticles can be thermally evolved at low temperature in air from 2 nm CuAu NPs or a mixture of Cu and Au nanoclusters while retaining the alloy characteristics (Supporting Information, Figure S1a,b). In addition to the well documented lower melting point for bulk gold−copper alloys (Supporting Information, Figure S1c,d), the melting curves calculated for the nanoalloys show that the melting temperatures are much lower than those for the bulk alloy and the component counterparts (Supporting Information, Figure S1c). This is consistent with the experimental observation.[26]

The fundamental basis for pulsed-laser sintering of metal NPs stems from the coupling of laser excitation with the surface plasmonic (SP) resonance of the metal NPs, producing highly localized heating in the NPs. For example, visible radiation of gold nanoparticles at surface plasmon resonant frequencies produces thermal energy where the temperature rise in an aqueous suspension of 20 nm gold particles irradiated by a laser at 514 nm is shown to increase in proportion

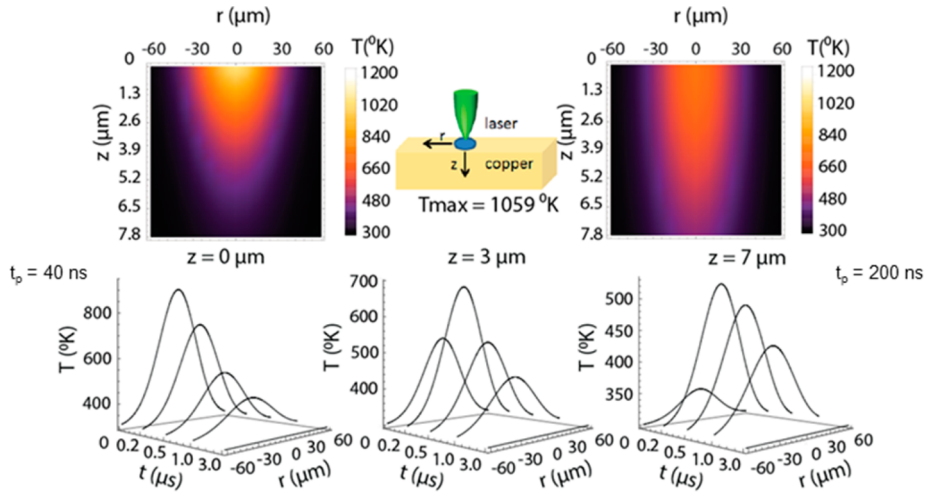

Figure 2. Calculated spatial temperature (*T*) profiles during (at 40 ns) and after (at 200 ns) 527 nm, 30-μJ, 100 ns radially symmetric laser with 50-μm diameter irradiation on 2 nm Cu NPs.

to incident laser power.[15] The heat and temperature rise generated by electromagnetic radiation of metal nanoparticles are shown to be enhanced under plasmon resonance and also to depend on the size, shape and assembly of the nanoparticles in a certain matrix.[16] The SP absorption depends on the composition of CuAu alloy,[25] as shown by simulation results based on Mie theory (Supporting Information, Figure S2), which are consistent with both previous theoretical simulations[30] and experimental results. The coupling of laser *via* the SP resonance depends on the laser wavelength and the composition of the nanoalloy. Absorption of 527 nm laser is larger for Au-rich nanoalloys, whereas absorption of 355 nm laser is larger for Cu-rich nanoalloys.

When a laser beam is irradiated, the SP resonance in NPs enhances laser light absorption,[31] thereby increasing temperature instantaneously (nanosecond scales).[32] Since laser sintering localizes heat only in the focal point, the sintered region can be small even down to a few micrometers. The spatiotemporal temperature profiles during and after laser sintering of copper NPs assuming constant thermal conductivity were calculated based on the work by Bechtel.[33] The spatiotemporal heat-conduction equation with a radially symmetric laser beam is given by

$$\nabla^2 T(r,z,t) - \frac{1}{k}\frac{\partial T(r,z,t)}{\partial t} = -\frac{A(r,z,t)}{K} \qquad (1)$$

where k is the thermal diffusivity and K is the thermal conductivity.$T(r,z,t)$ is the temperature and $A(r,z,t)$ is the net energy per unit volume per unit time generated within the medium (source term), where r, z, and t are the radial coordinate, the propagation distance from the surface, and the temporal coordinate, respectively. The source term $A(r,z,t)$ is given by

$$A(r,z,t) = I_m(1-R)\alpha \exp(-\alpha z) f(r) q(t) \qquad (2)$$

where I_m is the maximum incident irradiance intensity, R is the surface reflectivity, and α is the absorption coefficient of nanoparticles. $f(r) = \exp(-r^2/w^2)$ is the spatial profile of the laser irradiance with the (1/e) radius w and $q(t) = \exp(-t^2/\tau^2)$ is the temporal profile of the laser irradiance with the (1/e) radius τ. The spatiotemporal temperature distribution can be calculated by solving eq 1 considering sintering laser parameters. For laser light absorption by nanoparticles, we calculate a linear Mie absorption cross section of each nanoparticle which depends on parameters such as wavelength, size,[17] and an absorption coefficient based on the cross section and measured nanoparticle density.

Figure 2 shows 3-D temperature profiles when a 527 nm, 100 ns, 30-μJ laser pulse is incident on 2 nm diameter copper NPs with a 50-μm focal diameter. Temporally, the temperature (T) goes up to 1000 K at the surface ($z = 0$) during laser irradiation (i) and quick cooling occurs after the laser pulse such that T drops down to the threshold temperature ($T_{th} \sim 500$ K) of melting (ii) . This indicates that before the next laser pulse (1 ms pulse-to-pulse separation), T quickly goes down to room temperature. Spatially, T goes down from 1000 to 500 K about 5 μm away from the surface due to light attenuation *via* strong absorption by NPs, in good agreement with the measured thickness of sintered layers. To provide a more quantitative assessment, the thermal penetration depth through the nanoparticles is also considered in our simulation (Supporting Information, Figures S3 and S4). A simple 1-D spatiotemporal heat-conduction model is used to calculate the substrate effect on heat conduction, in which the temperature distribution $T(z, t)$ is a function of the depth from the surface of the nanoparticle ink layer (z), and the time (t), which considers the thermal conductivity (k), the specific heat capacity (c), and the density of the medium (ρ). For different nanoink–substrate interface spacing from the top of the ink layer, the result in Supporting Information Figure S3a is found to be quite comparable to the simulation result

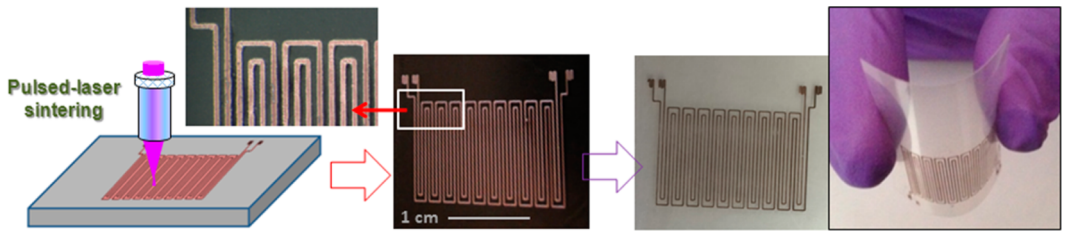

Figure 3. Pulsed-laser sintering process. Laser-sintering of $Cu_{53}Au_{47}$ nanoalloy printed PET substrate using a 355 nm laser (0.5 W, 100 kHz, 30 ns pulse width, and 70 mm/s laser moving speed). The time durations for the laser writing and ink removing to reveal the pattern (line length, 30 cm; width, 90 μm; and thickness, 3 μm) are 8 and 6 s, respectively.

considering only nanoparticle inks since the interface is far away (40 μm). In the case when the interface is closer to the surface (*i.e.*, 5 μm), the surface temperature $T(z = 0, t)$ decreases somewhat faster, indicating that the substrate contributes to lowering the ink temperature. However, it only slightly affects the temperature in a thin sintering layer near the interface. Nevertheless, the basic feature of the temperature decay profiles as a function of the depth (z) indicates that the thermal penetration depth into the substrate can be controlled by laser pulse duration and width.

For laser sintering of 2 nm $Cu_{90}Au_{10}$ NPs when the pulse duration Δt is varied (100 ns, 1 μs, and 1 ms) while maintaining the same peak power, T goes up as the pulse duration increases (Supporting Information, Figure S5), indicating that sintering with short pulse lasers has an advantage over longer and/or CW lasers since it minimizes thermal damages.

The laser sintering process involves scanning the focused pulsed laser beam over the nanoink-printed substrate using a computer-controlled program under a specific speed and power, followed by dissolving the unsintered inks (Figure 3). Line widths in the range of 80−400 μm, and thickness range from 1 to 5 μm can be easily generated, as revealed by AFM (Supporting Information, Figure S6). With the use of a laser moving speed of 70 mm/s, the CuAu microelectrode pattern (Figure 3) was generated in less than ~8 s (Supporting Information, Movie S1). The line thickness of ~2.5 μm, as determined by AFM, is very close to the estimated thickness (~2.9 μm). There is an improved effectiveness in sintering nanoalloy inks with 355 nm laser, in comparison with 527 nm laser, reflecting the effective laser absorption by the surface plasmonic band of nanoalloys. The less-uniform morphology and lower conductivity reflect the lack of effective coupling between the 527 nm laser and the surface plasmonic band of CuAu nanoparticles, as revealed by the calculation results. In contrast, use of a 355 nm pulsed laser was shown to be effective for sintering both Au and CuAu alloy nanoparticles on the different substrates. The morphology of the sintered lines of the CuAu alloy printed on PET (Supporting Information, Figure S6) is found to exhibit a smoother surface than that of the sintered Au. In addition to the subtle difference between the sintered Au and AuCu, sintering of copper nanoparticles was found to be difficult under the same ambient laser sintering condition due to the propensity of oxidation. Data shown in almost all studies of laser sintering or thermal sintering of copper nanoparticles were collected under inert or reductive atmosphere or with certain reactive additives in the nanoinks for subsequent reduction of the oxidized copper after sinteting.

While it is demonstrated that laser sintering can achieve very high resolution (down to a few nm) if inkjet printing and laser sintering are combined,[3] the focus of the present work is not on the resolution, rather on the correlation of sintered nanoinks with the laser sintering parameters and substrate parameters for which the sintered line width was used as a quantitative measure. The laser moving speed and the distance from the focus also influence the laser-sintering process on different substrates (Figure 4A). The line width increases with the distance from the focus, displaying an approximate linear relationship (Figure 4B), which agrees with a theoretical calculation of the beam diameter *vs* focus distance (Figure 4B, dashed line; Supporting Information, Figure S7). The line width decreases with laser moving speed (Figure 4C), suggesting that the decreased number of laser shots in given space at a high speed narrows the line width. Note that the use of tight focusing geometries can achieve a minimized focus size (Supporting Information, Figure S7) down to the diffraction limit (*i.e.*, the size of wavelength), which is expected to reduce the sintering feature size significantly.

Interestingly, the average line width on glass is consistently smaller than that on PET substrate (Figure 4B). This is, to our knowledge, the first example of this kind, and is believed to reflect the differences in mobility and adhesion of the particles on the different substrates. The sintering process is analyzed by considering Gibbs−Thomson relation, in which the size distribution depends on the interplay between the interparticle distances (*i.e.*, density), the thermal mobility of metal atoms on the surface, the interaction between the particles and the substrate, or the kinetic activation energy for metal atoms moving on the surface.[34] On the basis of classical nucleation theory and the Gibbs−Thomson relation,[35] the rate for the change of a metal particle's radius (R) can be

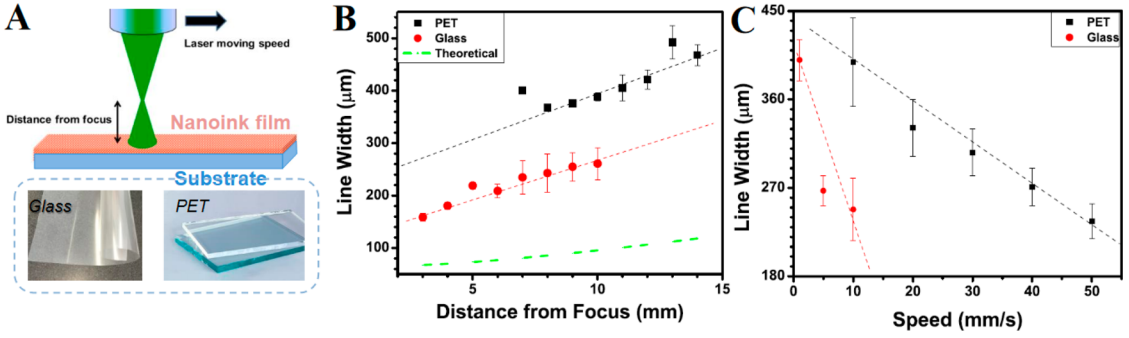

Figure 4. Dependencies of pulsed-laser sintered line width on laser focus distance, laser scan speed, and chemical nature of the substrate. (A) Scheme illustrating variations of the distance from the focus or the laser moving speed for nanoinks printed on two different substrates (PET and glass). (B) Plots of sintered line width *vs* the distance from the focus; green dashed line: calculated curve (Supporting Information, Figure S7). (C) Plots of the line width *vs* laser moving speed.

derived as

$$dR/dt = \frac{4\gamma\nu_P\Omega^2 \sin\theta}{kTR^2\upsilon a(2 - 3\cos\theta + \cos^3\theta)} \times e^{(-E_{tot}/kT)}\left(\frac{R}{R^*} - 1\right) \quad (3)$$

where γ is the surface free energy of the metal; Ω is the bulk metals volume per atom; E_{tot} is the metal's bulk sublimation enthalpy (ΔH_{sub}) minus the adsorption energy of a monomer on the support ($E_{ad}^{support}$), plus the diffusion activation energy of a metal monomer atom on the support ($E_{diff}^{support}$); k is Boltzmann's constant; T is the temperature of the substrate; υ is the heating rate; and R^* = 1/(average of 1/R for all particles). θ is the equilibrium contact angle of the metal particles with the support surface, ν_P is the prefactor in the rate constant for the elementary step, and a is the interatomic spacing in the metal. The rate of change of a metal particle's radius (R) is related to the total kinetic energy barrier (E_{tot}) and the contact angle of the metal particles with the support surface (θ). The contact angle for the initial capped gold NPs on PET is expected to be smaller than the contact angle for those on glass substrate, whereas the adhesion of particles (after removing the capping shells) on PET is expected to be smaller than the adhesion of those on glass, as supported by theoretical simulation (Supporting Information, Figure S8). Note that the impact of differences in specific heat and thermal diffusivity of the substrate on the sintering could also be considered in the above simulations (Supporting Information, Figure S4). For example, with the use of specific heat ~840 J kg^{-1} K^{-1} for glass substrate and ~1000 J kg^{-1} K^{-1} for PET, the ratio of temperature change between glass and PET will be ~1.2 under the same heating condition, suggesting that the temperature of glass will be only slightly higher than PET. Considering the thermal diffusivity of glass ~3.4 × 10^{-7} m^2/s, and of PET ~1.1 × 10^{-7} m^2/s, the ratio of temperature change between glass and PET will be ~3.1 under the same temperature curvature, suggesting that the temperature of glass will be higher than that of PET. In both considerations, the temperature of glass will be higher than that of PET, contributing to the particle size increase on glass being greater than that on PET, in agreement with the experimental result. Moreover, in light of recent literature 1-D model simulation for sintering silver nanoparticles on PEN substrate,[36] we attempted to correlate the nanoparticle sintering based on Gibbs–Thomson relation[35] and the thermal penetration depth under different laser fluence (Supporting Information, Figure S4), indicating again the contribution of the substrate to sintering is only at the very interface, and essentially insignificant in the substrate. Considering the very similar values of specific heat and thermal conductivity between PEN and PET, this trend should be applicable to PET substrate.

Laser sintering of nanoalloy inks on a PET substrate precoated with two metal films, *e.g.*, Au and Cr with subtle differences in surface binding energies, was studied to assess the substrate effect (Figure 5A). The degree of sintering (*i.e.*, particle size growth) is found to be greater on Cr than on Au substrates if the binding energies of CuAu to Au *vs* CuAu to Cr are considered for an estimate of the difference of activation energy barrier (Supporting Information, Figure S8). This is consistent with the clear transition from a wider line width on Cr to a narrower width on Au (Figure 5A), and the linear trends of the line width *vs* laser moving speeds (Figure 5B). This new finding has applications for writing circuits over substrates with complex surface properties.

As evidenced by XRD and XPS characterizations of the morphology and composition (Figure 6), the laser-sintered CuAu lines remain alloy characteristic with the degree of sintering being scaled inversely with the laser speed. For example, in contrast to the broad and unresolved peaks due to small size features (2 nm) before sintering, the XRD patterns after laser sintering reveal clearly resolved peaks that are characteristic of the gold–copper alloy character (Figure 6A). On the basis of *Bragg's Law*, the average lattice constant was estimated from the diffraction peaks to be 0.403–0.405 nm, falling in between Au lattice constant

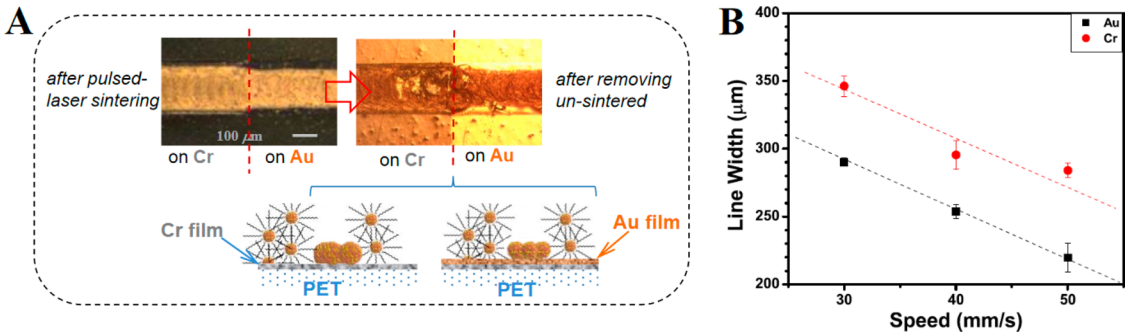

Figure 5. Dependencies of pulsed-laser sintered line width on chemical nature of the substrate. (A) Schemes and photos showing pulsed-laser sintering of CuAu NPs printed on PET coated with Cr and Au thin films. (B) Experimental plots of laser sintered line width *vs* laser moving speed for nanoalloy ($Cu_{53}Au_{47}$) printed on PET coated with Cr and Au films, measured from the portion of the line on Au (black squares and line) and that on Cr (red circles and line).

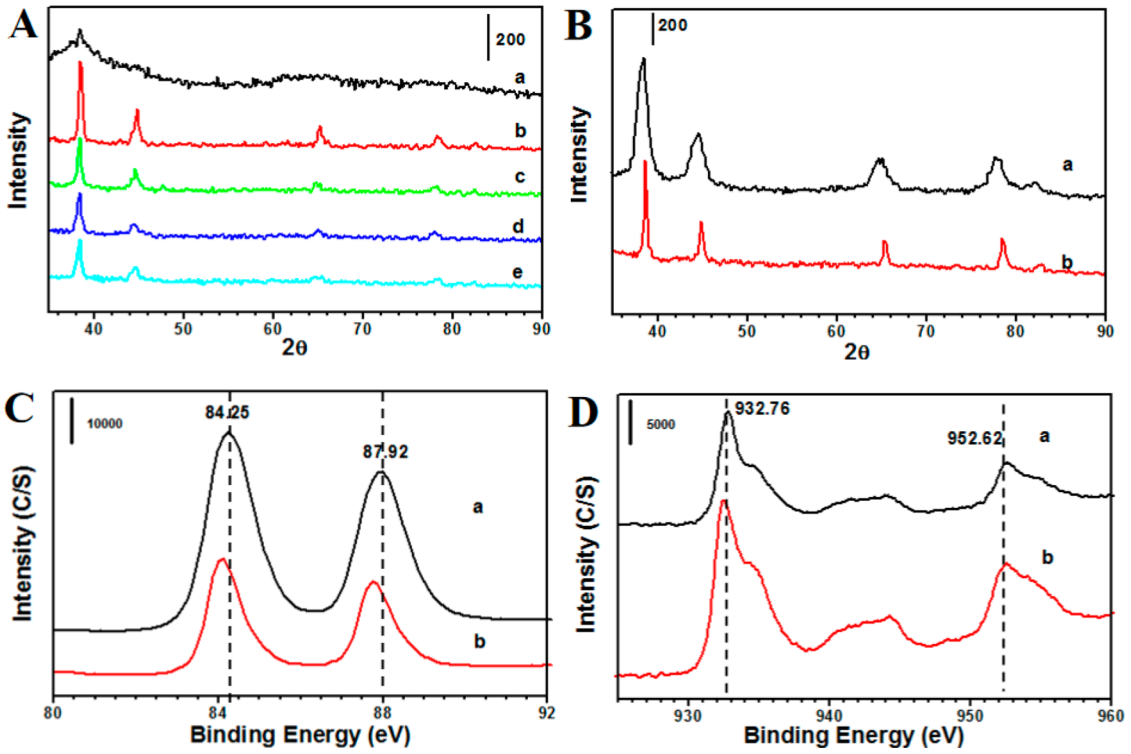

Figure 6. XRD patterns (A and B) and XPS spectra (C and D) for nanoink-printed films by pulsed-laser sintering in comparison with thermal sintering. (A) Comparison of XRD patterns for printed $Cu_{20}Au_{80}$ nanoalloys on glass between before laser sintering (a) and after laser sintering under different laser speed: 1 (b), 5 (c), 10 (d), and 20 mm/s (e). (B) Comparison of XRD patterns for printed $Cu_{30}Au_{70}$ nanoalloys after thermal sintering (a, black), and laser sintering (b, red). (C and D) Comparison of XPS spectra for printed $Cu_{67}Au_{33}$ nanoalloys on PET before (a) and after laser sintering (b) in regions of Au 4f (C) and Cu 2p (D).

(0.408 nm) and Cu lattice constant (0.360 nm). This is indicative of alloy character throughout the sintering process. The sintered alloy particle domain sizes calculated with *Scherrer* eq (10−18 nm upon changing the laser speed from 20 to 1 mm/s) showed a clear decrease of the domain size with an increase of laser-moving speed. This finding can be explained by the total heating time duration of the pulsed lasers on the nanoparticle inks during the laser-sintering process. The longer the heating time duration (*i.e.*, the number of laser shots), the higher the degree of sintering is. The XRD patterns for printed $Au_{70}Cu_{30}$ alloy nanoparticles are further compared between the pulsed-laser sintering and the thermal sintering (180 °C) (Figure 6B). In comparison with thermal sintering, the XRD peaks for the laser sintered nanoalloys are much narrower, showing larger particle domain sizes (>17 nm). An average lattice constant of 0.4069 nm was obtained for thermal sintering, whereas an average of 0.4043 nm was obtained for laser sintering of the same nanoalloy. This subtle difference reflects possibly a higher degree of sintering for Cu component in the alloy nanoparticles by laser sintering. Clearly, laser sintering is more effective than thermal sintering especially for the case of copper-rich nanoink printed films.

The propensity of oxidation of copper is clearly suppressed by the nanoscale alloying, in sharp contrast to commercial copper nanoinks under ambient conditions, which were supported by XPS analysis of the degree of surface oxidation before and after sintering by 355 nm pulsed laser (Figure 6C,D). The Cu 2p and Au 4f peak positions are largely identical, characteristic of reduced states of the two metals. A close examination of the peak position reveals a subtle shift (0.26 eV) to lower binding energy of the peaks for the sample after laser sintering. This shift is consistent with the removal of the capping molecules so that the metals on the sintered large-sized particles or domains are less positively charged in comparison with the thiolate-capped small-sized nanoparticles where the surface of Au or Cu on the nanoparticles is partially positively charged. For the unsintered AuCu nanoalloy, the detected surface Cu-to-Au ratio, 5.54/5.77 (*i.e.*, 49% Cu) is somewhat smaller than the Cu% in the bulk composition ($Au_{33}Cu_{67}$), whereas a value of 8.59/2.23 (*i.e.*, 79% Cu) detected after laser sintering is somewhat larger than the bulk composition, which is not unreasonable considering the surface sensitivity of XPS analysis. While the origin for the difference is not completely clear at this time, it is believed that a combination of the particle size increase and the different surface enrichment may be partially operative for the unsintered and sintered AuCu alloy nanoparticles. For the unsintered alloy nanoparticles, it is possible that the surface is slightly enriched with gold largely due to the more favorable gold−sulfur binding than the copper−sulfur binding.[26]

Taken together, the XRD and XPS results have led to three conclusions: (i) the morphology and composition of the sintered AuCu alloy remain alloys with domain sizes scaling inversely with the laser speed; (ii) laser sintering is more effective than thermal sintering, especially for nanoinks containing copper component; and (iii) the propensity of oxidation of Cu is prevented effectively by the alloying structure, which is a significant progress in comparison with many of the commercial copper nanoinks.

The resistivity for the pulsed-laser sintered nanoalloy lines on PET is about 1 order of magnitude higher than that for the bulk counterparts (bulk Cu: 1.7×10^{-8} Ω·m). For example, the two-probe measured resistivity is 6.8×10^{-7} Ω·m for the laser-written device on $Cu_{57}Au_{43}$ NPs on PET. The electrical properties also depend on laser speed and power. For Au NPs with 355 nm laser at different speeds, the resistivity increases with the speed, reflecting a lower degree of sintering at the higher speed. For printed Au NPs with 527 nm laser of different power, the resistivity gradually decreases with laser power, but there is a threshold of laser power, above which (>29 mW) laser penetration to the PET substrate occurs. As shown by bending fatigue test (Supporting Information, Movie S2), while the change of resistance in response to tensile bending showed a gradual increase from 2% to 20% after ~12 000 cycles, along with a 20% increase in resistance, the returned to its initial value after a few minutes demonstrated an excellent durability.

The laser-written microelectrode (LW-IME, in serpentine style) is tested as a flexible chemiresistor device, in which a sensing thin film is printed, consisting of a network of decanethiolate-capped Au NPs linked by 11-mercaptoundecanoic acid ($MUA\text{-}Au_{2nm}$)[28,37] (Figure 7A). The thermally activated electrical conductivity of the film is a function of particle size, interparticle distance and dielectric properties. It is exploited for detection of volatile organic compounds (VOCs), which is important for environmental monitoring of air pollution (*e.g.*, hexane, a toxic air containment associated with polyneuropathy in humans), but also of great interest for human breath sensing of biomarkers of various diseases (*e.g.*, acetone vapor associated with diabetes breath biomarker). The ability to detect these VOCs requires sensors with high sensitivity and selectivity.

As shown in Figure 7B,C, upon adsorption of VOCs, changes in interparticle distance and dielectric properties translate to a change in electrical conductivity with its sensitivity and selectivity depending on the molecular interaction. In comparison with photolithography-patterned interdigitated microelectrode (IME), the laser written nanoalloy IME shows a comparable increase in relative resistance change ($\Delta R/R$) in response to acetone and hexane vapors. With the same printed $MUA\text{-}Au_{2nm}$ sensing film, the response sensitivity for the laser-written IME is 2−4 times higher than that for the photolithagraphy-made IME. Note that the printed $MUA\text{-}Au_{2nm}$ thin film on IME device shows a response sensitivity of 2−4 times higher than self-assembled $MUA\text{-}Au_{2nm}$ film. Limit of detection is further lowered for the laser-sintered nanoalloy device, yielding 20−40 ppb for acetone under >90% relative humidity. The capability of highly sensitive detection of other VOCs[28,37] has also been demonstrated.

The difference in response sensitivity between hexane and acetone arises from a combination of the differences of the molecular interactions and the relative change in interparticle properties upon vapor adsorption into the film. The stronger hydrophobic interaction of hexane with the capping molecules (decanethiolates) and the lower dielectric medium properties lead to a greater change in $\Delta R/R$. On the basis of the different response sensitivities to these two vapors between LW-IME and PP-IME devices, principle component analysis (PCA) of the data (Figure 8) indicates that the VOCs can be effectively separated by a selective combination of the chemiresistor device parameters and the thin film nanostructural parameters. This finding is significant, demonstrating the viability of achieving sensor selectivity with a flexible array fabricated by a simple "nanoalloy printing−laser

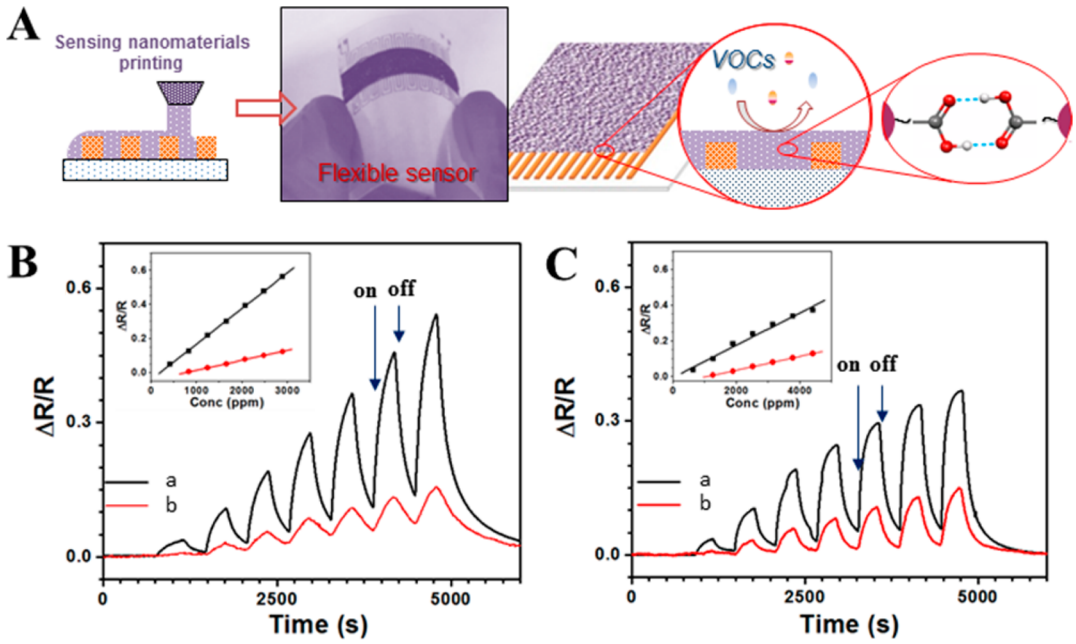

Figure 7. (A) A scheme illustration of printing a nanostructured sensing film (*e.g.*, MUA-linked Au nanoparticle thin film *via* interparticle hydrogen-bonding as illustrated by the far-right inset) on pulsed-laser written chemiresistor pattern for sensing VOCs. (B and C). Response profiles to VOCs for a printed MUA-linked Au nanoparticle thin film as sensing materials on laser-written $Cu_{57}Au_{43}$ interdigitated (in serpentine style) microelectrodes (LW-IME, a) device. VOC: acetone (B) and hexane (C) of different vapor concentrations (ppm (M)). The sensitivity for LW-IME is 4.0×10^{-6} for acetone and 9.3×10^{-6} ppm $(V)^{-1}$ for hexane. Data for printed MUA-$Au_{2\ nm}$ film on a photolithographically patterned IME (PP-IME, b, Cu/PET, red curve) are included for comparison (1.7×10^{-6} for acetone and 2.6×10^{-6} ppm $(V)^{-1}$ for hexane).

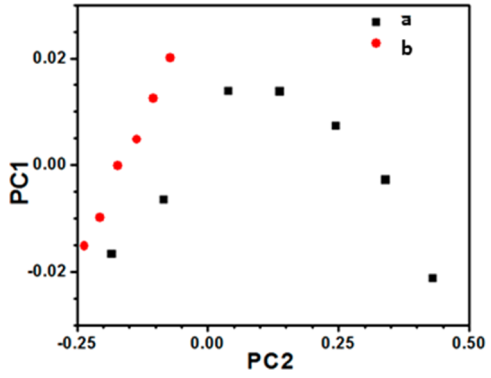

Figure 8. PCA scores plot of the response sensitivities to hexane (a, black) and acetone (b, red) in the PC1−PC2 plane.

sintering−nanostructure printing" process. This process can be general to many other nanostructured sensing materials, enabling the ability to easily construct sophisticated sensor array.

Moreover, this simple "nanoalloy printing−laser sintering−nanostructure printing" process could also allow easy integration of other components into the flexible device. One area of potential application is to couple this process to the fabrication of a flexible sensor powering system to enable stand-alone operation capability. This viability was examined by testing the laser-written nanoalloy microelectrode on PET as a footprint in a flexible Li-ion battery. The preliminary result of this test (Supporting Information, Figure S9) was indeed promising, demonstrating the feasibility of a flexible battery for powering the flexible sensors.

CONCLUSIONS

In conclusion, pulsed-laser writing of printed nanoalloys has demonstrated the ability to create footprints or patterns embedded in flexible sensor devices. Under ambient conditions, the propensity of oxidation of copper is effectively stopped by the nanoscale alloying, providing a promising lead to possibilities of exploring other nanoalloys for this scalable printing-writing technology. The laser written sensor coupled with printed sensing films is highly sensitive to VOCs, which could potentially be used as a stand-alone flexible sensor by integrating laser-written power in the device. Since pulsed-laser heating is well-targeted to the printed nanoalloys without hurting the substrate, the findings have significant implications to integration of pulsed-laser writing and nanoink printing as a fully printable and versatile process in roll-to-roll manufacturing of almost any flexible electronic device.

EXPERIMENTAL METHODS

Nanoalloy Synthesis and Nanoink Preparation. Copper−gold alloy nanoparticles encapsulated with decanethiolate (DT) monolayer shells with controlled size (~2 nm) and composition (Cu_nAu_{100-n} (n = 0−100)) were synthesized by modification of two-phase reduction of $AuCl_4^-$ and $CuBr_4^{2-}$, as described recently.[21,22]

For the device fabrication, the Au and CuAu alloy nanoparticles were redispersed in cyclohexane solution (0.39 g/mL). Doctor Blade was used to print the nanoink onto different substrates to achieve the desired thickness (glass, PET, metals, *etc.*). For printing sensing thin films, decanethiolate-capped gold nanoparticles were linked using 11-mercaptoundecanoic acid (MUA),[25,37] redispersed in an ethanol solution forming MUA-$Au_{2\ nm}$ nanoink, and then printed on the laser-written electrode device with controlled thickness.

Pulsed Laser Sintering Process. Two laser systems were used in this work. A pulsed green laser (527 nm) was used (Evolution 30 from Coherent; 1 kHz pulse frequency, 100 ns pulse duration, focused beam diameter size of 50 μm, and power $\leq$60 mW used). The second system is a pulsed UV laser (355 nm) system (Excellon's COBRA hybrid 7000 series; 100 kHz pulse frequency, 30 ns pulse duration, and power of 0.5 W used). The laser scanning speed was adjusted in the range of 0−100 mm/s with different distance from the focus.

Sensor Measurements. Computer-interfaced multichannel Keithley (Model 2700) instrument was used to measure the lateral resistance of the nanostructured thin films on the laser-written devices, which were housed in a Teflon chamber with tubing connections to vapor and N_2 sources (at 22 $\pm$ 1 °C). The concentration was controlled by bubbling dry N_2 gas through the solvent using a calibrated Aalborg mass-flow controller (AFC-2600). The vapor generating system consisted of multichannel module linked to different vapor sources.

Characterizations. XRD data were collected on a Philips X'Pert diffractometer using Cu Kα radiation (λ = 1.5418 Å). The measurements were done in reflection geometry and the diffraction (Bragg) angles 2θ were scanned at a step of 0.025°. TEM and high-resolution composition mapping were carried out using a JEOL JEM 2010F with an acceleration voltage of 200 kV and a routine point-to-point resolution of 0.194 nm, or an FEI Tecnai T12 Spirit Twin TEM/SEM electron microscope (120 kV). A Multimode Nano-Scope IIIa (Digital Instruments), equipped with an E scanner (maximum scan size = 100 μm), was utilized for AFM imaging. The pyramidal-shaped silicon nitride tip (Si_3N_4) on cantilever was used for contact-mode AFM measurement. XPS measurements were collected using a Physical Electronics Quantum 2000 scanning ESCA microprobe. This system uses a focused monochromatic Al Kα X-ray (1486.7 eV) source and a spherical section analyzer. The X-ray beam used was a 100 W, 100 mm diameter that was rastered over a 1.3 mm by 0.2 mm rectangle on the sample. Wide scan data was collected using a pass energy of 117.4 eV. The C 1s peak was used as an internal standard (284.8 eV) for the calibration of the binding energy.

Conflict of Interest: The authors declare no competing financial interest.

Acknowledgment. Part of preliminary work performed by Yvonne Xu and Kelly Cartwright is acknowledged. We thank Dr. Z. Xu for helpful discussion of PCA data analysis, and M. Engelhard for assistance in XPS analysis, which was performed using EMSL, a national scientific user facility sponsored by the DOE's Office of Biological and Environmental Research located at PNNL. The research is supported by the National Science Foundation (CMMI 1100736), and in part by SUNY NoE and SUNY Research Foundation Fund.

Supporting Information Available: Additional theoretical and experimental data. The Supporting Information is available free of charge on the ACS Publications website at DOI: 10.1021/acsnano.5b02704.

REFERENCES AND NOTES

1. Park, S.; Wang, G.; Cho, B.; Kim, Y.; Song, S.; Ji, Y.; Yoon, M.-H.; Lee, T. Flexible Molecular-Scale Electronic Devices. *Nat. Nanotechnol.* **2012**, *7*, 438–442.
2. Baca, A. J.; Ahn, J.-H.; Suun, Y.; Meitl, M. A.; Menard, E.; kim, H.-S.; Choi, W. M.; Kim, D.-H.; Huang, Y.; Rogers, J. A. Semiconductor Wires and Ribbons for High Performance Flexible Electronics. *Angew. Chem., Int. Ed.* **2008**, *47*, 5524–5542.
3. Son, Y.; Yeo, J.; Moon, H.; Lim, T. W.; Hong, S.; Nam, K. H.; Yoo, S.; Grigoropoulos, C. P.; Yang, D.-Y.; Ko, S. H. Nanoscale Electronics: Digital Fabrication by Direct Femtosecond Laser Processing of Metal Nanoparticles. *Adv. Mater.* **2011**, *23*, 3176.
4. Yeo, J.; Hong, S.; Lee, D.; Hotz, N.; Lee, M. T.; Grigoropoulos, C. P.; Ko, S. H. Next Generation Non-Vacuum, Maskless, Low Temperature Nanoparticle Ink Laser Digital Direct Metal Patterning for a Large Area Flexible Electronics. *PLoS One* **2012**, *7*, e42315.
5. Chun, K.-Y.; OH, Y.; Rho, J.; Ahn, J.-H.; Kim, Y.-J.; Choi, H. R.; Baik, S. Highly Conductive, Printable and Stretchable Composite Films of Carbon Nanotubes and Silver. *Nat. Nanotechnol.* **2010**, *5*, 853–857.
6. Yang, R.; Qin, Y.; Dai, L.; Wang, Z. L. Power Generation with Laterally Packaged Piezoelectric Fine Wires. *Nat. Nanotechnol.* **2009**, *4*, 34–39.
7. Son, D.; Lee, J.; Qiao, S.; Ghaffari, R.; Kim, J.; Lee, J. E.; Song, C.; Kim, S. J.; Lee, D. J.; Jun, S. W.; et al. Multifunctional Wearable Devices for Diagnosis and Therapy of Movement Disorders. *Nat. Nanotechnol.* **2014**, *9*, 397–404.
8. Dua, V.; Surwade, S. P.; Ammu, S.; Agnihotra, S. R.; Jain, S.; Roberts, K. E.; Park, S.; Ruoff, R. S.; Manohar, S. K. All-Organic Vapor Sensor Using Inkjet-Printed Reduced Graphene Oxide. *Angew. Chem., Int. Ed.* **2010**, *49*, 1–5.
9. Ko, S. H.; Pa, H.; Grigoropoulos, C. P.; Luscombe, C. K.; Poulikakos, D. Lithography-Free High-Resolution Organic Transistors on Polymer Substrate by Low Temperature Selective Laser Ablation of Inkjet Printed Nanoparticle Film. *Appl. Phys. A: Mater. Sci. Process.* **2008**, *92*, 579–587.
10. Joo, M.; Lee, B.; Jeong, S.; Lee, M. Comparative Studies on Thermal and Laser Sintering for Highly Conductive Cu Films Printable on Plastic Substrate. *Thin Solid Films* **2012**, *520*, 2878–2883.
11. Gaikwad, A. M.; Whiting, G. L.; Steingart, D. A.; Arias, A. C. Highly Flexible, Printed Alkaline Batteries Based on Mesh-Embedded Electrodes. *Adv. Mater.* **2011**, *23*, 3251–3255.
12. Cortie, M. B.; Coutts, M. J.; Ton-That, C.; Dowd, A.; Keast, V. J.; McDonagh, A. M. On the Coalescence of Nanoparticulate Gold Sinter Ink. *J. Phys. Chem. C* **2013**, *117*, 11377–11384.
13. Peng, P.; Hu, A.; Zhou, Y. Laser Sintering of Silver Nanoparticle Thin Films: Microstructure and Optical Properties. *Appl. Phys. A: Mater. Sci. Process.* **2012**, *108*, 685–691.
14. Auyeung, R. C. Y.; Kim, H.; Mathews, S. A.; Piqué, A. Laser Direct-Write of Metallic Nanoparticle Inks. *J. Laser Micro/Nanoeng.* **2007**, *2*, 21–25.
15. Roper, D. K.; Ahn, W.; Hoepfner, M. Microscale Heat Transfer Transduced by Surface Plasmon Resonant Gold Nanoparticles. *J. Phys. Chem. C* **2007**, *11*, 3636–3641.
16. Govorov, A. O.; Richardson, H. Generating Heat with Metal Nanoparticles. *Nano Today* **2007**, *2*, 30–38.
17. Kim, H. S.; Dhage, S. R.; Shim, D. E.; Hahn, H. T. Intense Pulsed Light Sintering of Copper Nanoink for Printed Electronics. *Appl. Phys. A: Mater. Sci. Process.* **2009**, *91*, 791–798.
18. Li, Y.; Wong, C. P. Monolayer Protection for Eletrochemical Migration Control in Silver Nanocomposite. *Appl. Phys. Lett.* **2006**, *89*, 112112.
19. Kumpulainen, T.; Pekkanen, J.; Valkama, J.; Laakso, J.; Tuokko, R.; Mäntysalo, M. Low Temperature Nanoparticle Sintering with Continuous Wave and Pulse Lasers. *Opt. Laser Technol.* **2011**, *43*, 570–576.
20. Halonen, E.; Heinonen, E.; Mäntysalo, M. The Effect of Laser Sintering Process Parameters on Cu Nanoparticle Ink in Room Conditions. *Opt. Photonics J.* **2013**, *3*, 40–44.
21. Lee, D. G.; Kim, D. K.; Moon, Y. J.; Moon, S. H. Effect of Laser-Induced Temperature on the Characteristics of Laser-Sintered Silver Nanoparticle Ink. *Nanotechnology* **2013**, *24*, 265702.
22. Zenou, M.; Ermak, O.; Saar, A.; Kotler, Z. Laser Sintering of Copper Nanoparticles. *J. Phys. D: Appl. Phys.* **2014**, *47*, 025501.
23. Joo, M.; Lee, B.; Jeong, S.; Lee, M. Comparative Studies on Thermal and Laser Sintering for Highly Conductive Cu Films Printable on Plastic Substrate. *Thin Solid Films* **2012**, *520*, 2878–2883.

24. Schroder, K. A.; McCool, S. C.; Furlan, W. F. Broadcast Photonic Curing of Metallic Nanoparticle Films. *NSTI Nanotech 2006, NSTI Nanotechnol. Conf. Trade Show* **2006**, *3*, 198–201.
25. Xu, Z. C.; Lai, E.; Shao-Horn, Y.; Hamad-Schifferli, K. Compositional Dependence of the Stability of AuCu Alloy Nanoparticles. *Chem. Commun.* **2012**, *48*, 5626–5628.
26. Yin, J.; Shan, S.; Yang, L.; Mott, D.; Malis, O.; Petkov, V.; Cai, F.; Ng, M. S.; Luo, J.; Chen, B. H.; et al. Gold-Copper Nanoparticles: Nanostructural Evolution and Bifunctional Catalytic Sites. *Chem. Mater.* **2012**, *24*, 4662–4674.
27. Yin, J.; Hu, P.; Luo, J.; Wang, L.; Cohen, M. F.; Zhong, C. J. Molecularly−Mediated Thin Film Assembly of Nanoparticles on Flexible Devices: Electrical Conductivity *vs.* Device Strains in Different Gas/Vapor Environment. *ACS Nano* **2011**, *5*, 6516–6526.
28. Wang, L.; Shi, X.; Kariuki, N. N.; Schadt, M.; Wang, G. R.; Rendeng, Q.; Choi, J.; Luo, J.; Lu, S.; Zhong, C. J. Array of Molecularly-Mediated Thin Film Assemblies of Nanoparticles: Correlation of Vapor Sensing with Interparticle Spatial Properties. *J. Am. Chem. Soc.* **2007**, *129*, 2161–2170.
29. Zhou, G.; Li, F.; Cheng, H.-M. Progress in Flexible Lithium Batteries and Future Prospects. *Energy Environ. Sci.* **2014**, *7*, 1307–1338.
30. Su, Y. H.; Wang, W. L. Surface Plasmon Resonance of Au-Cu Bimetallic Nanoparticles Predicted by a Quasi-Chmical Model. *Nanoscale Res. Lett.* **2013**, *8*, 408–413.
31. Shim, B.; Hays, G.; Zgadzaj, R.; Ditmire, T.; Downer, M. C. Enhanced Harmonic Generation from Expanding Clusters. *Phys. Rev. Lett.* **2007**, *98*, 123902.
32. Reiner, J. E.; Robertson, J. W. F.; Burden, D. L.; Burden, L. K.; Balijepalli, A.; Kasianowicz, J. J. Temperature Sculpting in Yoctoliter Volumes. *J. Am. Chem. Soc.* **2013**, *135*, 3087–3094.
33. Bechtel, J. H. Heating of Solid Targets with Laser Pulses. *J. Appl. Phys.* **1975**, *46*, 1585.
34. Campbell, C. T.; Parker, S. C.; Starr, D. E. The Effect of Size-Dependent Nanoparticle Energetics on Catalyst Sintering. *Science* **2002**, *298*, 811–814.
35. Luo, J.; Jones, V. W.; Han, L.; Maye, M. M.; Kariuki, N.; Zhong, C. J. AFM Probing of Thermal Activation of Molecularly-Linked Nanoparticle Assembly. *J. Phys. Chem. B* **2004**, *108*, 9669–9677.
36. Theodorakos, I.; Zacharatos, F.; Geremia, R.; Karnakis, D.; Zergioti, I. Selective Laser Sintering of Ag Nanoparticles Ink for Applications in Flexible Electronics. *Appl. Surf. Sci.* **2014**, *336*, 157–162.
37. Luo, L.; Luo, J.; Wang, L.; Shi, X.; Yin, J.; Crew, E.; Lu, S.; Lesperance, L. M.; Zhong, C. J. Nanoparticle-Structured Thin Film Sensor Arrays for Breath Sensing. *Sens. Actuators, B* **2012**, *161*, 845–854.